Research Article | Vol. 10, No. 1 | 1 Jan 2019 | BIOMEDICAL OPTICS EXPRESS 226
Biomedical Optics EXPRESS

Handheld optical palpation of turbid tissue with motion-artifact correction

Brooke Krajancich,[1,2] Andrea Curatolo,[1,2,3] Qi Fang,[1,2] Renate Zilkens,[1,4] Benjamin F. Dessauvagie,[5,6] Christobel M. Saunders,[4,7,8] and Brendan F. Kennedy[1,2,*]

[1]*BRITElab, Harry Perkins Institute of Medical Research, QEII Medical Centre, Nedlands and Centre for Medical Research, The University of Western Australia, Perth, Western Australia, 6009, Australia*
[2]*Department of Electrical, Electronic & Computer Engineering, School of Engineering, The University of Western Australia, 35 Stirling Highway, Perth, Western Australia, 6009, Australia*
[3]*Current address: Visual Optics and Biophotonics Laboratory, Instituto de Óptica "Daza de Valdés", Consejo Superior de Investigaciones Cientificas (IO, CSIC), C/Serrano, 121, Madrid 28006, Spain*
[4]*Division of Surgery, Medical School, The University of Western Australia, 35 Stirling Highway, Perth, Western Australia, 6009, Australia*
[5]*PathWest, Fiona Stanley Hospital, 11 Robin Warren Drive, Murdoch, Western Australia, 6150, Australia*
[6]*School of Pathology and Laboratory Medicine, The University of Western Australia, 35 Stirling Highway, Perth, Western Australia, 6009, Australia*
[7]*Breast Centre, Fiona Stanley Hospital, 11 Robin Warren Drive, Murdoch, Western Australia, 6150, Australia*
[8]*Breast Clinic, Royal Perth Hospital, 197 Wellington Street, Perth, Western Australia, 6000, Australia*
**brendan.kennedy@uwa.edu.au*

Abstract: Handheld imaging probes are needed to extend the clinical translation of optical elastography to *in vivo* applications, yet such probes have received little attention. In this paper, we present the first demonstration of optical palpation using a handheld probe. Optical palpation is a variant of optical elastography that uses three-dimensional optical coherence tomography (3D-OCT) to provide maps of stress at the tissue surface under static compression. Using this technique, stiff features present beneath the surface of turbid tissues are identified, providing mechanical contrast complementary to the optical contrast provided by OCT. However, during handheld operation, relative motion between the probe and the tissue can induce motion artifact, causing spatial distortion of 3D-OCT and in turn, optical palpation images. We overcome this issue using a novel, dual-function bi-layer that provides both a fiducial marker for co-registration and a compliant section for estimation of the stress at the tissue surface. Co-registration of digital photographs of the bi-layer laid out over the tissue surface is used to measure and correct for motion in the lateral (*xy*) plane. We also demonstrate, for the first time, that optical palpation can be used as a method for monitoring pressure applied to the tissue during handheld operation, thus providing a more repeatable and robust imaging technique between different users. Handheld optical palpation is demonstrated on a structured phantom, *in vivo* human skin and excised human breast tissue. In each case, image quality comparable to bench-top 3D-OCT and optical palpation is achieved.

1. Introduction

Optical elastography is a suite of light-based imaging techniques developed to characterise and map the mechanical properties of biological tissue by measuring the deformation in response to a mechanical load [1]. These techniques hold promise for a wide range of applications in areas such as oncology [2], ophthalmology [3] and dermatology [4], for example, in differentiating tumor from healthy tissue during cancer surgery [5–7] and in tracking the progression of burn scars [8].

#348836 https://doi.org/10.1364/BOE.10.000226
Journal © 2019 Received 22 Oct 2018; revised 2 Dec 2018; accepted 3 Dec 2018; published 18 Dec 2018

Biomedical Optics EXPRESS

The ability to perform optical elastography with a handheld probe is needed for extension to clinical use [1], yet such imaging is challenging, largely because of motion artifact distorting the image and causing a time-dependent variation in mechanical loading. There have been a number of *in vivo* demonstrations of optical elastography [8–11], however these have largely been performed by benchtop systems or semi-mounted probes, artificially removing motion artifact. Transition of optical elastography to handheld probes operated freely by the user is key to enabling wide application to *in vivo* and clinical scenarios, as is the case in ultrasound elastography [12–14]. Recently, a handheld optical coherence elastography (OCE) probe using manual compression has been demonstrated on excised tissue [15]. In this approach, motion artifact along the depth axis is accounted for by utilizing a noise-tolerant vector-method [16] for strain estimation and calculating an inter-frame cumulative strain. As this approach used phase-sensitive detection, it is very sensitive to motion artifact. To overcome this, in [15], hundreds of B-scans were averaged to generate elastograms, making it challenging to implement clinically. In addition, as this technique is not readily extendable to 3D, and therefore, *en face* imaging, it is limited in its ability to survey large tissue areas in clinically relevant timeframes.

In this paper, we demonstrate, for the first time, optical palpation, a variant of optical elastography, using a handheld probe unsupported by any apparatus. Optical palpation [17] is a tactile imaging technique that generates maps, referred to as optical palpograms, of the axial stress at the surface of tissue under static compression. The stress is calculated by measuring the deformation of a translucent, compliant layer with known mechanical properties using three-dimensional optical coherence tomography (3D-OCT). Elevated regions of stress indicate stiffer underlying features, thus if compression is kept approximately constant between samples, stress may be used to distinguish tissue types. Particularly in turbid tissues, where optical contrast alone is often insufficient to distinguish features of interest [18], optical palpation has been demonstrated to enhance visualization by providing complementary mechanical contrast [19,9]. Importantly, as optical palpation does not rely on dense oversampling, as is the case with phase-sensitive approaches [15,20], acquisition times can be as rapid as in standard 3D-OCT. In addition, as optical palpation provides *en face* images, it enables large surface areas (up to 16 × 16 mm [19]) to be scanned in one acquisition.

Key to realizing freehand optical palpation is overcoming motion artifact, caused by movement of the user's hand during scanning, or in the case of *in vivo* imaging, involuntary movement of the patient. Relative motion between the probe and tissue typically causes spatial distortion of 3D-OCT volumes which, in turn, distorts optical palpograms. This can degrade the appearance and size of tissue features, for example, sub-surface blood vessels and areas of tumor, and needs to be corrected to ensure both faithful reconstruction of tissue structure, and proper estimation of surface stress. In optical elastography to date, motion-artifact has only been accounted for along the depth axis, and motion correction of handheld optical palpograms has not yet been demonstrated. There has, however, been several demonstrations of motion correction in 3D-OCT [21–25], based on information either encoded in the OCT images themselves, or provided by some concurrent tool. One such study used the registration of multiple scanning laser ophthalmoscope images acquired during the handheld 3D-OCT scans to measure and correct for motion in the lateral (*xy*) plane [26]. This registration, however, relied on the detection and alignment of vessels, and as such, this result may not be extendable to imaging of more turbid tissue, in which such key features may not be present. Another method estimates and corrects for motion using a fiducial marker, a rigid object of known shape and size laid out over the tissue of interest, and image correlation of consecutively acquired B-scans [27]. Although this removes the need for key features on the tissue surface, the rigid metal fiducial marker would obscure the mechanical contrast of the tissue, making it unsuitable for extension to optical palpation.

Biomedical Optics EXPRESS

To demonstrate handheld optical palpation, we overcome these pivotal issues by implementing a novel, dual-function bi-layer, simultaneously performing both stress measurement and motion correction. Placed on the tissue surface, a compliant layer of soft material can be deformed in order to perform optical palpation, while a fiducial marker is embedded in a secondary top layer. This top layer is made of stiffer silicone to ensure that it is not deformed by hand motion. In our approach, motion correction is performed using a digital camera in-built in the handheld OCT probe to track motion in the lateral plane, relative to the tissue surface. Relative offsets and rotations between successive OCT B-scans are measured by simultaneously acquiring a photograph of the tissue surface for each B-scan in the OCT volume. We then run a pixel-intensity correlation algorithm on successive pairs of photographs, facilitating lateral motion estimation to within ~16 μm. The corresponding B-scan is then transformed accordingly, for each B-scan in the OCT volume, forming a more accurate representation of the tissue geometry. This motion-corrected 3D-OCT volume enables us to generate motion-corrected optical palpograms, providing mechanical contrast complementary to the optical contrast provided by OCT.

We also show, for the first time, that optical palpation can be used to monitor pressure applied to the tissue surface during handheld scanning. This is an important development for handheld OCT in general, as it has been reported that pressure can affect the rate of blood flow and can warp structures imaged by OCT [28,29]. In addition, our technique can be used to ensure that applied pressure is below the pain threshold of human subjects (0.4 MPa [30]), to avoid discomfort [10]. We achieve this by computing and comparing the average stress in the area of interest, enabling more repeatable and consistent OCT imaging with handheld probes across different patients and operators.

To demonstrate handheld optical palpation, we present results from a structured phantom, *in vivo* scans of human skin, and excised human breast tissue. In each case, we show substantial reduction in motion artifact in 3D-OCT and hence optical palpation, providing accurate contrast of key tissue features. We also demonstrate optical palpation as a method for monitoring pressure applied to the tissue by the user, providing insight into the ability to compare scans. We believe that this work is an important development towards routine optical elastography with handheld probes, expediting development towards *in vivo* clinical application.

2. Methods

2.1 The handheld OCT probe

Scanning was performed using a commercial, spectral-domain OCT system (TELESTO III, Thorlabs Inc., Newton, NJ, USA) operating at a center wavelength of 1300 nm. The full width at half maximum (FWHM) axial and lateral resolutions were measured to be 5.5 μm (in free space) and 14.4 μm, respectively. The objective scanning lens (LK30, Thorlabs) has a working distance of 22 mm and the acquired imaging volume was 7 × 7 × 2.5 mm in x, y and z, respectively. The sample arm comprised a handheld OCT probe (OCTH-1300, Thorlabs). Figure 1(a) shows a photograph of the probe, with overlaid axes which can be used to describe motion relative to the tissue; six degrees of freedom, three axes of translation (x, y, z), corresponding to the fast (x), slow (y) and depth (z) scan directions, respectively, and three rotational directions (pitch, yaw, roll) which pivot around these axes. A piezoelectric ring actuator (PA), similar to that previously used for optical coherence elastography (OCE) [21], is fixed to the probe using a threaded connection, giving the probe a total weight of ~0.3 kg. Although OCE was not performed in this study, this setup is designed to enable extension to such imaging in the future. A VIS-NIR AR coated glass imaging window (Edmund Optics) of diameter 20 mm and thickness 2 mm was attached to the ring actuator using wax. To perform scanning, contact is made between the window and the bi-layer, as described in Sec. 2.3, which is placed on the tissue surface. The reference mirror was removed from the handheld

Biomedical Optics EXPRESS

probe to facilitate a common-path configuration, with the reflected beam from the surface of the glass imaging window in contact with the bi-layer used as the reference reflection, as described previously [17,31].

A schematic diagram of the optical layout is provided in Fig. 1(b). The handheld OCT probe contains a 5 megapixel charge-coupled device (CCD) camera. This camera shares the same optical path as the OCT beam but records an image with a larger field of view than the 7 mm × 7 mm *en face* OCT area; constricted to a 13 mm diameter circle by the hollow area of the ring actuator. The camera captures photographs at a maximum rate of 6 frames per second, with a pixel size of 6.2 μm.

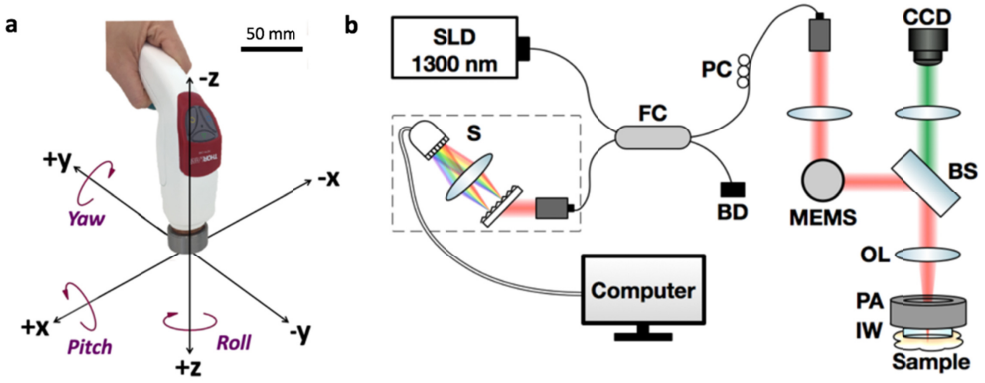

Fig. 1. Handheld probe used for optical palpation. (a) Photograph of the probe, with overlaid illustration of the six degrees of freedom. The probe body has dimensions 158 × 39 × 107 mm (L × W × H). (b) Schematic layout of the optical path in the handheld probe. SLD, superluminescent diode. PC, polarization controller. FC, fiber coupler. BD, beam dump. S, spectrometer. MEMS, microelectromechanical mirror system. BS, beam splitter. CCD, charge-coupled device. PA, piezoelectric actuator. IW, glass imaging window. OL, objective lens.

2.2 Optical palpation

To perform optical palpation, a translucent compliant silicone sensor is compressed, between the tissue and an imaging window. The deformed thickness of the layer is measured from a 3D-OCT scan, by detecting the layer/tissue interface using a Canny-based edge detection algorithm on each of the OCT B-scans. Then, strain, *i.e.* the change in thickness divided by the original thickness, at each lateral position in the layer is calculated [9,17]. Local stress values are estimated from the known stress-strain curve of the compliant layer under the assumption that the stress field within the layer is uniform and uniaxial, and the friction of the layer interfaces is low [17]. Mapping these stress values with their lateral locations gives an image referred to here as an optical palpogram.

2.3 Dual-function bi-layer fabrication

Key to successful demonstration of handheld optical palpation was the design and implementation of a dual-function bi-layer, enabling both stress estimation at the tissue surface, and tracking of the relative motion between the handheld probe and the tissue.

To assist in motion tracking, a circular fiducial marker was made by cutting a 6 mm square out of a plastic reinforcement sticker for hole-punched pages and coloring it in black with a permanent marker. As shown in Fig. 2(a), this marker was embedded in a transparent silicone layer fabricated from Elastosil RT601 (Wacker, Germany) to assist in fixing its position relative to the tissue surface.

Biomedical Optics EXPRESS

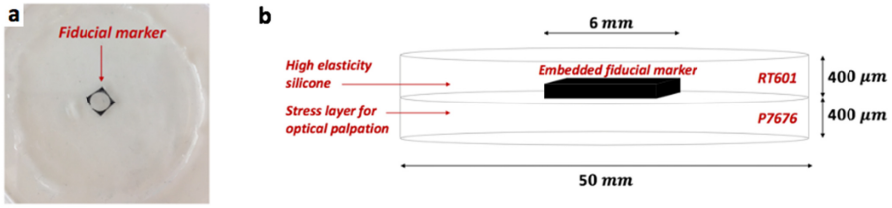

Fig. 2. Transparent silicone layer with embedded fiducial marker. (a) Top-down view photograph. (b) Schematic illustrating the structure and dimensions of the bi-layer.

As described in Section 2.2, optical palpation relies on deformation being introduced to the layer. However, in order to use it as a key feature for tracking motion, we require that the silicone surrounding the fiducial marker does not deform during a scan. As illustrated in Fig. 2(b), we achieve both of these requirements by creating a bi-layer material. Using methods outlined previously [32], we first cure the fiducial marker in a thin layer of rigid silicone (Elastosil RT601, Wacker, Germany), with a measured elasticity of ~4.9 MPa. A layer of softer silicone (Elastosil P7676, Wacker, Germany), with a measured elasticity of ~ 6 kPa , is then cured to the rigid layer, to enable optical palpation to be performed.

2.4 Structured phantom fabrication

To test our method on a known material, a structured phantom was also fabricated, using various combinations of silicone elastomers, to have a diameter of 50 mm and a thickness of 9 mm, using techniques described in detail previously [32]. The phantom contained a stiff (elasticity ≈ 4.9 MPa) inclusion fabricated using Elastosil RT601 in a matrix of softer (elasticity ≈ 6 kPa) Elastosil P7676. The inclusion was a ~1 × 1 × 1 mm cube, located ~ 0.5 mm below the phantom surface. To introduce optical scattering, titanium dioxide (TiO_2) particles (Sigma Aldrich 232033) with a mean diameter of <5 μm were added to both the bulk material (0.5 mg/mL) and the inclusion (3 mg/mL).

2.5 Data acquisition protocol

Prior to imaging, both sides of the silicone layer were lubricated with Elastosil AK50 silicone oil (Wacker, Germany) both to partially match the refractive index and to reduce friction at the layer/window and layer/tissue interfaces. Using one hand, the handheld OCT probe was then placed in contact with the tissue with moderate compression, while the other hand was used to steady the layer on the tissue. Custom software was used to acquire the data. The OCT probe was configured to capture a photograph concurrently with each OCT B-scan acquisition. In this way, each B-scan in the volume is associated with a corresponding photograph, which depicts the *en face* position of the fiducial marker with respect to the probe, and equivalently, the probe with respect to the tissue. Thus, an OCT B-scan rate of 6 Hz was chosen for the convenience of matching the maximum frame rate set by the in-built camera. Setting 808 B-scans per volume, 808 photographs are captured over a scan time of ~2 minutes. This image acquisition protocol is illustrated in Fig. 3.

Biomedical Optics EXPRESS

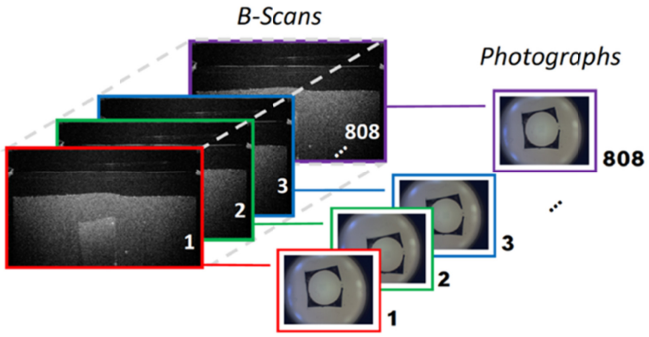

Fig. 3. Schematic of photograph capture with respect to B-scan acquisition.

2.6 Photographs for measuring motion

Acquiring photographs of the tissue surface during scanning provides a mechanism to quantify shifts that occur in the lateral plane: accounting for shifts in x, y and roll (see Fig. 1(a)). This can be accomplished by estimating the geometric transformation, in the form of a matrix, that maps the features in each successive photograph back to the placement of the same features in the first photograph (arbitrarily chosen as the stationary reference frame), *i.e.*, co-registration.

These 807 different transformations, T_n, were calculated using an in-built image co-registration algorithm in Matlab (Mathworks, USA). Assuming that the silicone layer stays in contact and is stationary with respect to the tissue, the fiducial marker provides a distinctive feature that assists in the accuracy of this optimum transformation calculation.

Unlike in ophthalmology, for applications in turbid tissues, the OCT imaging probe typically makes contact with the tissue surface. Furthermore, the moderate compression applied for optical palpation can assist in controlling vertical motion of the probe. Independent testing of pitch and yaw of the probe axis during the time of a 3D-OCT scan was conducted using two video cameras mounted on orthogonal planes (xz- and yz-plane) to monitor probe motion along these axes. Both tilt directions were determined to have minimal effect on the xy-plane deformation, being equivalent to shifts less than the lateral resolution of the OCT system, for up to 2.5 mm deep into the tissue. This meant that drift about the x- and y-axis within the scan time was limited to below 0.5°. Moreover, pressure was applied as normal to the specimen surface as possible, to avoid artificial stress gradients. Unlike OCE, optical palpation does not require phase-sensitive detection, and as such, motion in z was also seen to have negligible effect. Slip of the hand over the tissue surface, however, was significant, causing considerable motion artifact in the lateral plane (*i.e.*, on the *en face* OCT images). As such, our technique focuses on correcting motion in x, y and roll directions and considers motion in z, pitch and yaw directions to be negligible.

2.7 Correcting 3D-OCT data

In order to correct 3D-OCT, and in turn, optical palpograms, the geometric transformations calculated using the photographs need to be applied to OCT. Thus, a transformation, P, that maps each *en face* OCT pixel to its corresponding position in the probe photograph, and vice versa, was determined.

We demonstrate our motion correction technique in Fig. 4, using a handheld scan of a structured phantom. Taking any *en face* plane (a depth of ~0.8 mm below the phantom surface is shown in Fig. 4(a)), a particular B-scan (demonstrated for B-scan 600) is mapped to its location in the associated photograph (shown in Fig. 4(b)), using P. We then map this location to its co-registered position in Photograph 1, using T_n (T_{600} in this case). Finally, we map this back to the corresponding OCT coordinate location, and now motion-corrected

Biomedical Optics EXPRESS

position, using P^{-1}. Mapping all B-scans in this way generates the motion-corrected *en face* OCT scatterplot shown in Fig. 4(c). This figure illustrates that, depending on the motion experienced, the distance between scanned locations can exceed that of the lateral resolution, resulting in irregular coverage of the tissue. Thus, a best estimate of the OCT intensity in these areas is obtained by 2D interpolation and cropping to give the final output image shown in Fig. 4(d). Since, by previous findings, only lateral motion is significant, each *en face* OCT slice can be transformed separately and identically. In this way, an entire 3D-OCT scan can be corrected for motion artifact.

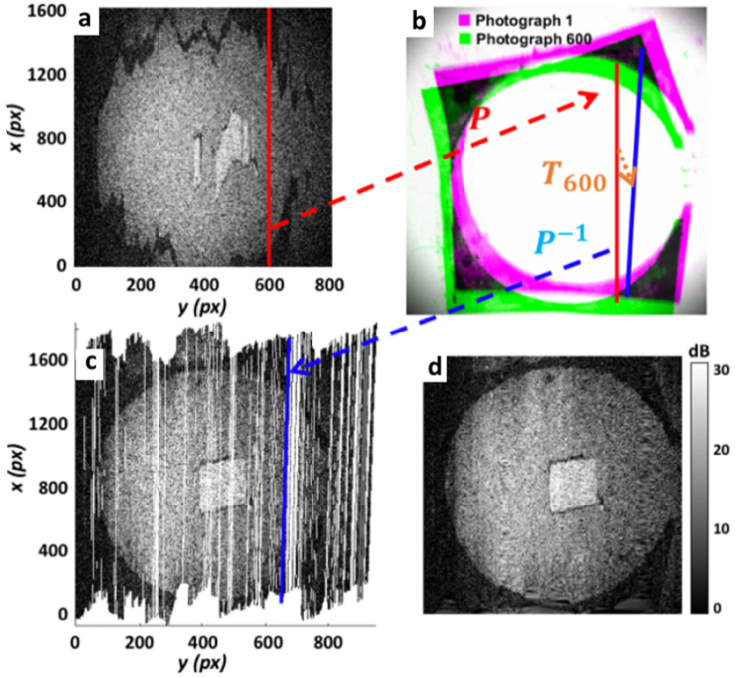

Fig. 4. Illustration demonstrating the motion correction technique. (a) B-scan 600 is selected to demonstrate transformations applied to motion-correct its position. (b) It is first transformed to its lateral position in Photograph 600, shown in green, then mapped its co-registered position in Photograph 1, shown in purple, using T_{600}. (c) Finally, this is mapped back to its corresponding OCT coordinate location, now motion-corrected. Mapping all B-scans in this way, with their associated co-registration transformation (T_n), generates the underlying *en face* OCT scatterplot shown. 2D interpolation and cropping of this scatterplot generates the final output motion-corrected *en face* OCT image in (d).

2.8 Accuracy of photograph correction technique

To demonstrate the accuracy of using photographs to measure lateral motion, motorized translation stages (Thorlabs NRT100) were used to introduce preset motion. The silicone layer was lubricated on both sides with silicone oil, and was placed on the structured phantom. A 3D-printed plastic casing was utilized to rigidly fix the handheld OCT probe in light contact with the layer, and the stages were set to translate at a constant speed of 15 μm/s in both *x* and *y* directions. Acquisition was set such that 500 photographs were taken at a rate of 6 Hz.

After cropping, each of the successive 500 photographs were then co-registered to the first photograph. Figure 5(a) shows Photograph 250 (in purple) overlaid on Photograph 1 (in green), and Fig. 5(b) shows this overlay after Photograph 250 has been co-registered to Photograph 1. The rigid motion between photographs is highlighted in orange. Extracting the

Biomedical Optics EXPRESS

calculated x and y translations from each transformation matrix and plotting against time allows comparison against the known translation stage speed, as shown in Figs. 5(c) and 5(d). These plots indicate close agreement between the position values calculated by photograph co-registration and a known reference. Calculating the standard deviation of the residuals about the expected values and the line of best fit gave an absolute accuracy of 15.8 µm and 15.5 µm, and a precision of 10.6 µm and 11.5 µm, for x and y respectively. This indicates an accuracy to within a few pixels. However, the stage manufacturer specifies an absolute on-axis accuracy of 15.29 µm [33], suggesting that our method is accurate to within the tolerance of the stages.

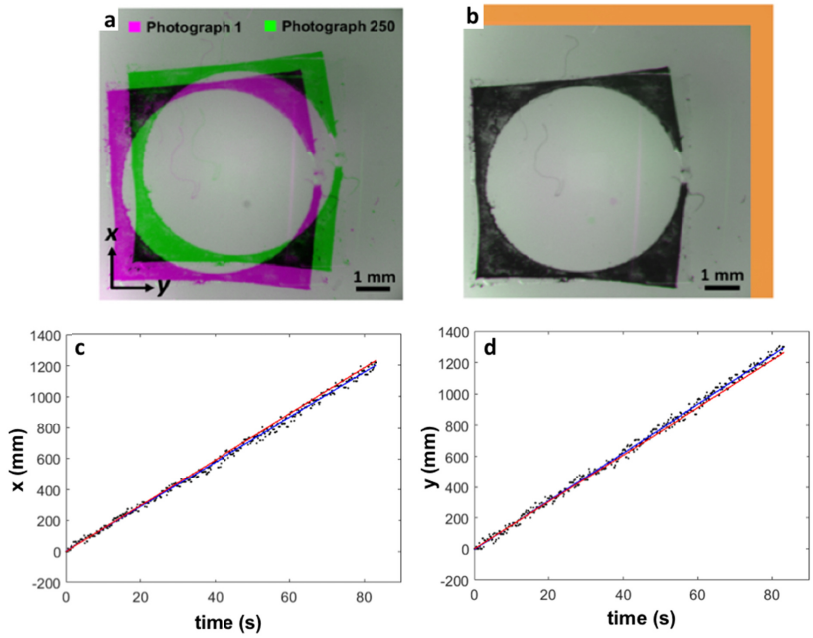

Fig. 5. Testing the accuracy of photograph co-registration. (a) Photograph 250 (green) overlaid on Photograph 1 (purple). (b) Photograph 250 co-registered and overlaid on Photograph 1. The area highlighted in orange shows movement of Photograph 250 from its original to new location. Graphs showing (c) x-translation and (d) y-translation calculated by photograph co-registration, the corresponding least squares line of best fit (blue line) and expected positions based on stage translation speed (red line).

3. Results

3.1 Structured phantom

Figure 6 shows the results of our approach on a structured silicone phantom. Figures 6(a)-6(c) show plots of x, y and roll hand motion, respectively, as estimated by the co-registration of the photographs taken during the handheld scan with respect to the phantom. The maximum shifts in x and y, and roll, relative to the start of the scan were of ~0.8 mm, ~1.5 mm and 2.1°, respectively. Figure 6(d) shows an *en face* OCT image taken from a depth of ~0.6 mm below the phantom surface. Acquired with the handheld OCT probe mounted on the benchtop, this image is free from motion-artifact. As such, the accurate shape of the fiducial marker and the square inclusion can be identified by their comparatively low and high OCT intensities, respectively. Figure 6(e) shows a corresponding OCT image acquired during handheld operation of the probe. The fiducial marker and the inclusion can be readily distinguished from the bulk by OCT intensity, but are distorted in shape due to motion of the probe relative to the phantom during the scan. Using our motion correction technique to transform this *en*

Biomedical Optics EXPRESS

face OCT depth, gives the image in Fig. 6(f). It can be seen that the correction provides an accurate reconstruction, as indicated by the circular shape of the fiducial marker. Due to the difficulty of scanning exactly the same location between handheld and mounted scenarios, a quantitative comparison with Fig. 6(d) is challenging, however a visual comparison reveals that the square shape of the inclusion has been reconstructed well. Several artifacts (A) are visible in Fig. 6(f), caused by inaccurate performance of interpolation when sudden motion of the hand has created an area of limited sampling. Since this phantom result was used to demonstrate the motion correction technique in Section 2.6, the spatial locations that were truly sampled during this scan can be seen in Fig. 4(c). Examination of this scatterplot reveals that drift in the x direction has seen the bottom edge of the fiducial marker not scanned and sudden motion in the y direction has caused an area of particularly scarce sampling towards the end of the scan. A lack of data limits the accuracy of interpolation, creating the artifacts (A) observed. The dark artifact (D) seen in Fig. 6(f) is a consequence of (Petzval) field curvature [34] effects from the LK30 achromatic doublet lens, causing lower signal-to-noise ratio (SNR) at the edges of the uncorrected OCT image. If, after the first few B-scans are captured, the operator's hand slips momentarily towards the positive y direction (as indicated by the arrow in Fig. 6(b)), then a more central region of the phantom is actually being sampled under field curvature aberration. Therefore, motion correcting the position of these B-scans can cause discontinuous OCT intensity (D), even when the phantom is homogeneous.

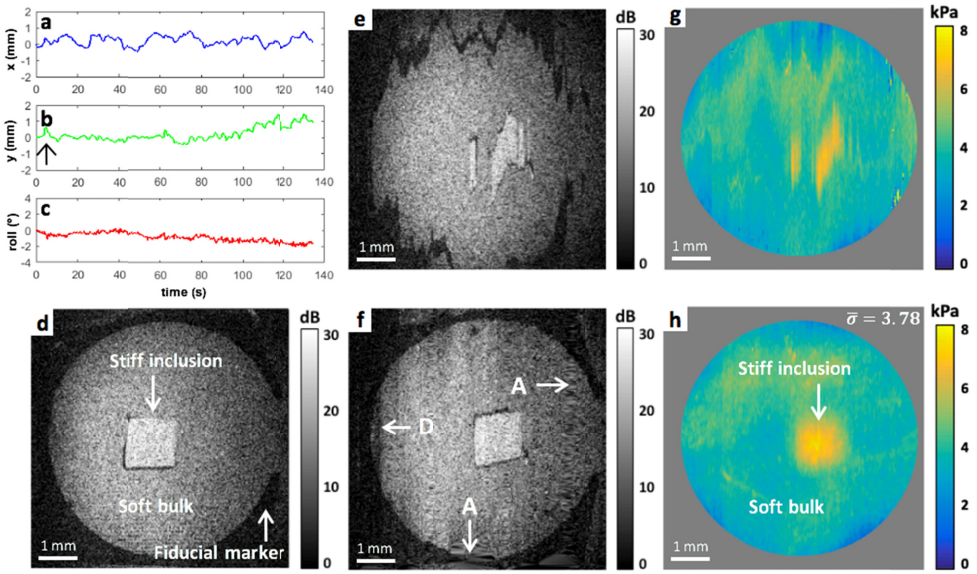

Fig. 6. Structured phantom. Plots of hand motion in (a) x, (b) y, and (c) roll directions, as measured by co-registering digital photographs captured by the OCT probe during scanning. (d) *En face* OCT at ~0.6 mm below the phantom surface, acquired with the handheld probe mounted on the benchtop, for a motion-artifact-free reference. Corresponding *en face* OCT image acquired in handheld (e) uncorrected, and (f) motion-corrected. (g) Uncorrected and (h) corresponding motion-corrected optical palpograms. The area outside of the fiducial marker has been masked out (in grey). $\bar{\sigma}$ is the average stress in kPa, and equivalently, pressure applied to the tissue during the scan. A, interpolation inaccuracy artifacts. D, field curvature artifact.

Figure 6(g) shows the uncorrected optical palpogram, distorted analogously to the uncorrected *en face* OCT image shown in Fig. 6(e), such that the correct shape of the inclusion cannot be determined. Using the motion-corrected 3D-OCT volume to generate the optical palpogram provides the result shown in Fig. 6(h). In both Figs. 6(g) and 6(h), the area outside the fiducial marker has been masked in grey. The inclusion is clearly identified by

Biomedical Optics EXPRESS

higher stress (~7 kPa) than the surrounding phantom material (~3 kPa), and its geometry is now consistent with the motion-corrected *en face* OCT image shown in Fig. 6(f). The average stress (or pressure), $\bar{\sigma}$, applied by the user during this scan is 3.78 kPa, calculated by averaging all stress values in the cropped optical palpogram. This value is useful in quantitatively guiding operators with applying adequate pre-load compression and assessing the ability to compare with other handheld scans of this phantom. Since optical palpation only relies on 3D-OCT to measure the deformation of the transparent compliant layer, it is less susceptible to error caused by small, localized OCT SNR variations. As such, the image artifacts (A,D), highlighted in Fig. 6(f), are not noticeable in Fig. 6(h).

3.2 Human skin

Figure 7 shows an *in vivo* handheld scan of the fingertip of a 21-year-old Caucasian female. The silicone layer was placed on the finger, with care taken to minimize slip during scanning. Figure 7(a) shows an uncorrected *en face* OCT image at a depth of ~0.4 mm below the skin surface. The fingerprint pattern can be identified by the stripe-like texture and the fiducial marker by its low OCT intensity, however, the shape of both is clearly distorted by hand motion during the scan. Transforming this image using our motion correction technique generates the image shown in Fig. 7(b). The circular shape of the fiducial marker is accurately reconstructed, and the lines of the fingerprint are now more easily recognizable. The small disruption in this pattern (A) is likely caused by the fiducial marker moving slightly with respect to the skin during the scan. This distorts the correction of the underlying tissue as the photograph co-registration preferentially aligns the fiducial marker in each photograph, due to its high contrast.

Figure 7(c) shows the uncorrected optical palpogram, and demonstrates similar distortion to the *en face* OCT image (Fig. 7(a)). The area outside of the fiducial marker has been masked in grey. Processing the motion-corrected 3D-OCT volume for optical palpation provides the optical palpogram shown in Fig. 7(d). This result can be used to see that the operator applied less pressure to the fingertip than the structured phantom (shown in Fig. 6), an average of 2.91 kPa. The fingerprint pattern can be identified in the image by the stress contrast caused mainly by the ridges and troughs of the finger pad, *i.e.*, surface topology. Figure 7(e) shows a photograph of the fingertip with the fiducial marker in place. The inset highlights the correspondence of both the corrected OCT and optical palpograms to the area scanned. Additionally, this photograph shows a small horizontal crease line (C) present on the fingertip; not readily visible in the OCT image but revealed by optical palpation. Scattered small vertical lines of high stress (E) are also present, indicating areas where the automatic algorithm for compliant layer/tissue edge detection, used in the calculation of stress (see Section 2.1), failed due to optical artifacts near the layer-tissue interface.

Biomedical Optics EXPRESS

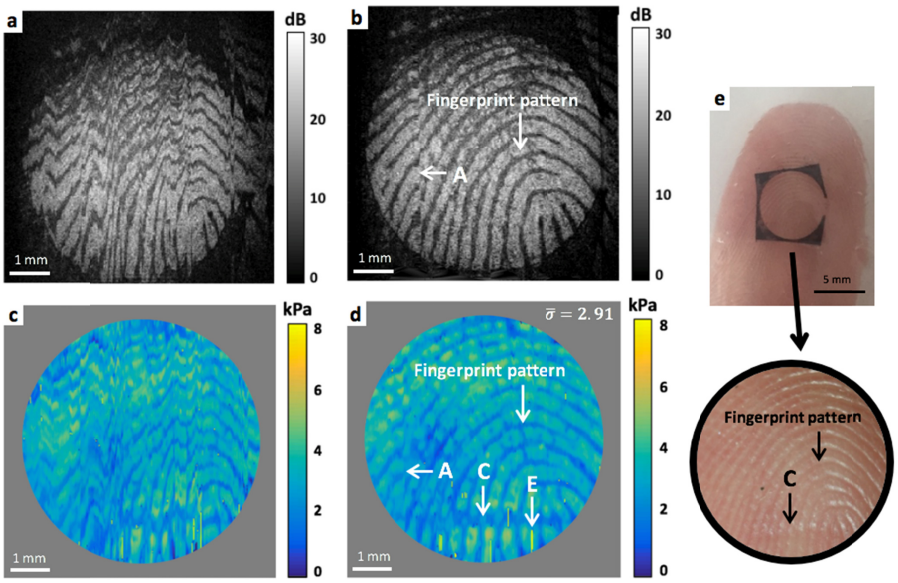

Fig. 7. Human fingertip. (a) Uncorrected *en face* OCT image at ~0.4 mm below skin surface and (b) corresponding motion-corrected OCT image. (c) Uncorrected and (d) corresponding motion corrected optical palpograms. The area outside of the fiducial marker has been masked out (in grey). $\bar{\sigma}$ is the average stress in kPa, and equivalently, pressure applied to the tissue during the scan. (e) Photograph of the fingertip with the fiducial marker in place. The inset highlights the region scanned by OCT. A, alignment artifact. C, crease in the skin on the fingertip. E. stress estimation artifacts.

3.3 Human breast tissue

A sample of freshly excised human breast tissue was obtained from a mastectomy procedure, carried out at Fiona Stanley Hospital, Western Australia. Informed consent was obtained from the patient, and all testing was conducted under ethics approved by the South Metropolitan Heath Service, Western Australia Human Research Ethics Committee (FSH-2015-032). Following surgery, the specimen was transferred from the operating theater to the clinical pathology laboratory for scanning with the handheld probe. The silicone layer was placed over the tissue sample, which had an approximate size of 30 mm × 35 mm × 8 mm, as shown in Fig. 8(a). The specimen scanned here was extracted from the location of a previous surgery, and contained a prominent region of fibrosis (F), corresponding to a well-formed surgical scar. A small area of interest was chosen for scanning, as indicated by the placement of the fiducial marker in Fig. 8(a). Figure 8(b) shows a wide-field OCT image of the specimen taken by a benchtop scanning head, as in previous work [35], with the position of the fiducial marker overlaid in orange. After scanning, the specimen was immediately returned for histopathological analysis in two sections, as shown in Fig. 8(c), revealing adipose (P), the fibrosis (F), and a small nerve (N) in the selected area. The wider field of view of the bench-top scan facilitates accurate co-registration of the smaller handheld OCT images with this histology.

Figure 8(d) shows the motion-corrected *en face* OCT image at a depth of ~0.1 mm below the tissue surface. Although the first edge of the fiducial marker was not scanned, due to difficulty in centering the marker with respect to the scanning area, it is clear that the overall shape has been accurately reconstructed, and that the underlying tissue appears significantly less spatially distorted. Comparing the bench-top scan in Fig. 8(b) to the handheld scan, it is clear that the motion-corrected image shows the same tissue micro-architecture. Similar to the scan of the structured phantom (Fig. 6), small artifacts (A) caused by inaccurate interpolation

Biomedical Optics EXPRESS

in areas of insufficient sampling occur on the edges of the image can be seen in Fig. 8(d). A section of lower SNR B-scans (D) is also present, again due to discontinuity caused by field curvature effects. However, unlike with the structured phantom, the presence of heterogeneous structures help to highlight the success of the reconstruction despite the artifact.

Figure 8(e) shows the corrected optical palpogram, calculated using the motion corrected 3D-OCT volume. Calculating the average stress in the cropped region, 3.15 kPa, indicates that the user applied slightly more pressure than for the fingerprint scan. This image more readily highlights areas of fibrosis (F), which are expected to be stiffer than surrounding stroma and adipose. In particular, optical palpation clearly identifies the location of the small nerve (N), which exhibits relatively low optical contrast in the OCT image in Fig. 8(d), demonstrating the value of complementary mechanical contrast. Again, small variations in OCT SNR are unlikely to affect the compliant layer deformation measurement, and hence the artifacts (A, D) in Fig. 8(d) are not noticeable in the corresponding optical palpogram. Small vertical lines of high stress (E) are present at the edges of the image due to localized failure of the stress estimation algorithm, but do not affect structures in the main area of interest.

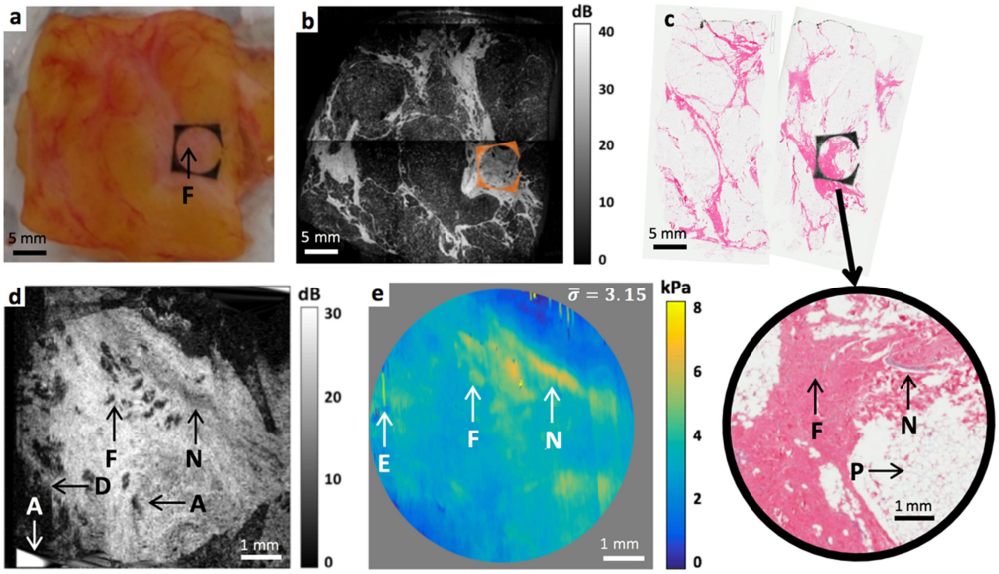

Fig. 8. Excised human breast tissue. (a) Specimen photograph with the fiducial marker in place. (b) Wide-field OCT image taken with a benchtop scanning head. The position of the fiducial marker has been overlaid (in orange). (c) Histology with the inset highlighting the region scanned by OCT. (d) Motion-corrected *en face* OCT image at ~0.1 mm below the tissue surface (e) Motion-corrected optical palpogram. The area outside of the fiducial marker has been masked in grey. $\bar{\sigma}$ is the average stress in kPa, and equivalently, pressure applied to the tissue during the scan. A, interpolation inaccuracy artifact. D, field curvature artifact. E, stress estimation artifacts. F, fibrosis from previous surgery. N, nerve. P, adipose.

Analyzing the histology shown in Fig. 8(c) shows agreement with the tissue types, in particular the nerve feature shown in Figs. 8(d) and 8(e), although positioning and relative sizes differ. Histological processing involves chemical fixation with formaldehyde, which often causes shrinkage and shape distortion. Furthermore, compression of the handheld tissue with the handheld probe can cause small distortions in the shape and locations of features. We note that this issue is less prominent for larger field-of-views, as in Fig. 8(b), and results presented in previous studies [19,35], since corresponding features become easier to identify.

Biomedical Optics EXPRESS

4. Discussion

The first demonstration of handheld optical palpation is presented in this paper. A main challenge we overcame was correction of operator- and tissue-induced motion artifact occurring during the scan. Importantly, in this study, the operator used a contact probe held freely in their hand. This is in contrast to prior demonstrations of optical palpation which used a support apparatus, such as an articulating mechanical arm [9] or mechanical stages [10] which are cumbersome for use in clinical applications.

Unlike for *x*, *y*, and roll motion, independent testing of *z*, pitch and yaw motion, while scanning with the OCT probe in contact with turbid tissue, revealed negligible motion-artifact on the 3D-OCT signal intensity. For pitch and yaw, this was confirmed in the structured phantom scan, by the consistent *en face* location of the inclusion edges throughout motion-corrected OCT volume. Comparisons of *y*-*z* profiles of the motion-corrected and mounted phantom scan, also confirmed negligible *z*-shifts. The handheld OCT probe used for this testing was fitted with an actuator to enable future extension to OCE [20] and quantitative micro-elastography [31] which rely on the fidelity of 3D-OCT scans. Since these techniques rely on phase-sensitive detection, they are significantly more sensitive to motion in *z*, as in the recent paper by Zaitsev *et al.* [15], than optical palpation. In ongoing work, we will assess existing and novel methods to also account for *z*-motion in OCE, and the possibility of extending our motion correction technique to image strain and elasticity using a handheld OCT probe.

Unlike in many previously demonstrated motion correction approaches for 3D-OCT, we do not rely on SNR or contrast in the underlying OCT data for performing motion correction, increasing versatility across different tissues types and OCT scanning approaches. By design, the technique does, however, assume that OCT intensity values are determined only by the optical backscattering of points sampled. Field curvature effects from the lens in the off-the-shelf handheld OCT probe, used in this demonstration, therefore caused small artifacts (D) in the motion corrected images (see Figs. 6(f) and 8(d)). This effect could be readily removed by cropping pixels at the edges of the 7 mm × 7 mm uncorrected *en face* OCT image or by using an f-theta corrected telecentric lens. The use of external hardware, *i.e.*, the in-built CCD camera, for motion tracking, also allows for the robust correction of large positional shifts. We demonstrate correction of up to 1.5 mm among B-scans (see Fig. 6(b)), limited primarily by the fiducial marker staying within the camera field of view. The ability to correct for hand motion is, however, limited by the 6 Hz sampling rate and a co-registration accuracy of within ~16 μm, with higher frequency and small magnitude hand motion unable to be accounted for.

The use of a dual-function bi-layer is key to the robust correction demonstrated, enabling the decoupling of the accuracy of surface tracking and properties of the underlying tissue, since it removes the need to resolve features in photographs and OCT images. It also provides an easy visual check that the correction has succeeded. However, this is based on the assumption that the fiducial marker does not move relative to the tissue surface during the scan. The occurrence of such motion will cause incorrect alignment of the underlying tissue, as seen by the alignment artifact (A) in Fig. 7(b), since the photograph co-registration will favor aligning the fiducial markers. Thus, care must be taken to ensure that the bi-layer remains stationary with respect to the tissue during acquisition. We also note that the fiducial marker can present a potential disadvantage in reducing the effective field of view of OCT, optical palpation, and tissue surface photographs. Another issue for the compliant silicone layer used for optical palpation is the potential presence of negative stress, when the layer is compressed against uneven surface tissues. As the layer is incompressible, it has a tendency to expand into softer or cavernous areas e.g. the troughs of the fingerprint (see Fig. 7(e)), resulting in small negative stresses being calculated. More generally, surface topology can create stress contrast that may not be a direct consequence of the mechanical properties of the underlying tissue, as in the case of the fingerprint (see Fig. 7(e)). This could potentially

Biomedical Optics EXPRESS

obscure the desired contrast in optical palpation by complicating the direct relationship between stress and stiffness. However, higher fidelity stiffness contrast can be found by employing quantitative micro-elastography [35] and extending this motion-correction technique to it. Meanwhile, incorrect surface stress estimation in palpograms, obtained under the assumptions that the stress field within the compliant section of the bi-layer is uniform and uniaxial, and the interface friction is low could also be overcome in future work by extending previously demonstrated computational optical palpation to *in vivo* work [36].

Routine use of this technique in a clinical setting will likely require substantially faster volume acquisition. With the current approach of conveniently matching the camera frame and B-scan rates, we were limited to a maximum B-scan frequency of 6 Hz, but B-scan rates >10 kHz have been demonstrated [37]. The installation of a higher frame rate digital camera would enable this technique to be adapted to faster acquisition times. Alternatively, the technique could be adapted such that a photograph is captured every few B-scans, rather than every B-scan, and motion for B-scans between photographs could be estimated by interpolation. Since increasing the B-scan frequency increases the data acquired before detectable movement occurs, this would also eliminate much of the interpolation artifacts caused by insufficient sampling (as seen in Fig. 4(c)). Although much of the motion artifact demonstrated in this paper could be accounted for by a faster imaging system, it is important to consider that all scans were acquired by engineers who were consciously trying to hold the OCT probe stationary. It is anticipated that clinical scanning scenarios, such as *in vivo* scanning of a surgical cavity by a surgeon, will result in substantially increased bulk motion. Thus, even with faster scanning speeds, we anticipate that motion correction will play an important role in ensuring fidelity to tissue features.

Computation time also has important implications for the feasibility of our approach to handheld 3D-OCT and optical palpation in clinical applications, with the current processing time of a few hours requiring significant reduction. The majority of this time can be attributed to co-registering 807 photographs with the current off-the-shelf algorithm, chosen to enable proof-of-concept demonstration. Optimizing this photograph co-registration algorithm has the potential to greatly reduce this processing time, for example, by co-registering only a small window from each photograph or by choosing a feature tracking technique. This processing time could be also significantly reduced by re-implementing the code in C + + , which is much faster than the current Matlab implementation, and moving to GPU-accelerated processing [38].

5. Conclusion

Handheld imaging probes are needed to extend clinical applications of optical elastography to *in vivo* scenarios, yet are challenging to implement, largely because of motion artifact. In this paper, we present the first demonstration of optical palpation, a variant of optical elastography, with a handheld probe, without any form of supporting apparatus. Key to enabling this demonstration was the development of a dual-function bi-layer, providing both a fiducial marker for tracking and correcting for lateral hand motion, and a compliant section for estimating stress at the tissue surface. We also demonstrate, for the first time, that optical palpation can be used as a method for measuring pressure applied to the tissue during handheld operation, thus providing a more repeatable and robust imaging technique between different users. An off-the-shelf handheld OCT probe was used to successfully demonstrate this approach on a structured phantom, *in vivo* human skin and excised human breast tissue. All *en face* OCT images showed greatly reduced motion artifact, even when almost 1.5 mm of motion occurred during a scan, and optical palpation was shown to be valuable in contrasting features. Future work will involve integration with faster OCT scanning, incorporation of live applied pressure readings and extension for use in other optical elastography techniques. This work is an important step towards developing optical elastography towards routine clinical use.

Biomedical Optics EXPRESS

Funding

Australian Research Council; Cancer Council, Western Australia; OncoRes Medical.

Disclosures

BFK: OncoRes Medical (F,I), AC and CMS: OncoRes Medical (I). The other authors declare that there are no conflicts of interest related to this article.

References

1. B. F. Kennedy, P. Wijesinghe, and D. D. Sampson, "The emergence of optical elastography in biomedicine," Nat. Photonics **11**(4), 215–221 (2017).
2. X. Liang, A. L. Oldenburg, V. Crecea, E. J. Chaney, and S. A. Boppart, "Optical micro-scale mapping of dynamic biomechanical tissue properties," Opt. Express **16**(15), 11052–11065 (2008).
3. R. K. Manapuram, S. R. Aglyamov, F. M. Monediado, M. Mashiatulla, J. Li, S. Y. Emelianov, and K. V. Larin, "In vivo estimation of elastic wave parameters using phase-stabilized swept source optical coherence elastography," J. Biomed. Opt. **17**(10), 100501 (2012).
4. B. F. Kennedy, X. Liang, S. G. Adie, D. K. Gerstmann, B. C. Quirk, S. A. Boppart, and D. D. Sampson, "In vivo three-dimensional optical coherence elastography," Opt. Express **19**(7), 6623–6634 (2011).
5. B. F. Kennedy, R. A. McLaughlin, K. M. Kennedy, L. Chin, P. Wijesinghe, A. Curatolo, A. Tien, M. Ronald, B. Latham, C. M. Saunders, and D. D. Sampson, "Investigation of Optical Coherence Microelastography as a Method to Visualize Cancers in Human Breast Tissue," Cancer Res. **75**(16), 3236–3245 (2015).
6. W. M. Allen, L. Chin, P. Wijesinghe, R. W. Kirk, B. Latham, D. D. Sampson, C. M. Saunders, and B. F. Kennedy, "Wide-field optical coherence micro-elastography for intraoperative assessment of human breast cancer margins," Biomed. Opt. Express **7**(10), 4139–4153 (2016).
7. C. Li, G. Guan, Y. Ling, Y.-T. Hsu, S. Song, J. T.-J. Huang, S. Lang, R. K. Wang, Z. Huang, and G. Nabi, "Detection and characterisation of biopsy tissue using quantitative optical coherence elastography (OCE) in men with suspected prostate cancer," Cancer Lett. **357**(1), 121–128 (2015).
8. S. Es'haghian, P. Gong, K. Kennedy, P. Wijesinghe, D. D. Sampson, R. A. McLaughlin, and B. Kennedy, "In vivo optical elastography: Stress and strain imaging of human skin lesions," Proc. SPIE **9327**, 93270C (2015).
9. S. Es'haghian, K. M. Kennedy, P. Gong, D. D. Sampson, R. A. McLaughlin, and B. F. Kennedy, "Optical palpation in vivo: imaging human skin lesions using mechanical contrast," J. Biomed. Opt. **20**(1), 016013 (2015).
10. S. Es'haghian, K. M. Kennedy, P. Gong, Q. Li, L. Chin, P. Wijesinghe, D. D. Sampson, R. A. McLaughlin, and B. F. Kennedy, "*In vivo* volumetric quantitative micro-elastography of human skin," Biomed. Opt. Express **8**(5), 2458–2471 (2017).
11. B. F. Kennedy, T. R. Hillman, R. A. McLaughlin, B. C. Quirk, and D. D. Sampson, "In vivo dynamic optical coherence elastography using a ring actuator," Opt. Express **17**(24), 21762–21772 (2009).
12. K. Chino, R. Akagi, M. Dohi, S. Fukashiro, and H. Takahashi, "Reliability and validity of quantifying absolute muscle hardness using ultrasound elastography," PLoS One **7**(9), e45764 (2012).
13. S. Wojcinski, J. Dupont, W. Schmidt, M. Cassel, and P. Hillemanns, "Real-time ultrasound elastography in 180 axillary lymph nodes: elasticity distribution in healthy lymph nodes and prediction of breast cancer metastases," BMC Med. Imaging **12**(1), 35 (2012).
14. A. Kuzmin, A. M. Zakrzewski, B. W. Anthony, and V. Lempitsky, "Multi-frame elastography using a handheld force-controlled ultrasound probe," IEEE Trans. Ultrason. Ferroelectr. Freq. Control **62**(8), 1486–1500 (2015).
15. A. A. Sovetsky, A. L. Matveyev, L. A. Matveev, D. V. Shabanov, and V. Y. Zaitsev, "Manually-operated compressional optical coherence elastography with effective aperiodic averaging: demonstrations for corneal and cartilaginous tissues," Laser Phys. Lett. **15**(8), 085602 (2018).
16. A. L. Matveyev, L. A. Matveev, A. A. Sovetsky, G. V. Gelikonov, A. A. Moiseev, and V. Y. Zaitsev, "Vector method for strain estimation in phase-sensitive optical coherence elastography," Laser Phys. Lett. **15**(6), 065603 (2018).
17. K. M. Kennedy, S. Es'haghian, L. Chin, R. A. McLaughlin, D. D. Sampson, and B. F. Kennedy, "Optical palpation: optical coherence tomography-based tactile imaging using a compliant sensor," Opt. Lett. **39**(10), 3014–3017 (2014).
18. X. Liang, B. W. Graf, and S. A. Boppart, "Imaging engineered tissues using structural and functional optical coherence tomography," J. Biophotonics **2**(11), 643–655 (2009).
19. W. M. Allen, P. Wijesinghe, B. F. Dessauvagie, B. Latham, C. M. Saunders, and B. F. Kennedy, "Optical palpation for the visualization of tumor in human breast tissue," J. Biophotonics **0**(0), e201800180 (2018).
20. B. F. Kennedy, R. A. McLaughlin, K. M. Kennedy, L. Chin, A. Curatolo, A. Tien, B. Latham, C. M. Saunders, and D. D. Sampson, "Optical coherence micro-elastography: mechanical-contrast imaging of tissue microstructure," Biomed. Opt. Express **5**(7), 2113–2124 (2014).
21. B. Antony, M. D. Abràmoff, L. Tang, W. D. Ramdas, J. R. Vingerling, N. M. Jansonius, K. Lee, Y. H. Kwon, M. Sonka, and M. K. Garvin, "Automated 3-D method for the correction of axial artifacts in spectral-domain optical coherence tomography images," Biomed. Opt. Express **2**(8), 2403–2416 (2011).

Biomedical Optics EXPRESS

22. R. J. Zawadzki, A. R. Fuller, S. S. Choi, D. F. Wiley, B. Hamann, and J. S. Werner, "Correction of motion artifacts and scanning beam distortions in 3D ophthalmic optical coherence tomography imaging," in *Ophthalmic Technologies XVII* (International Society for Optics and Photonics, 2007), **6426**, p. 642607.
23. B. Potsaid, I. Gorczynska, V. J. Srinivasan, Y. Chen, J. Jiang, A. Cable, and J. G. Fujimoto, "Ultrahigh speed spectral / Fourier domain OCT ophthalmic imaging at 70,000 to 312,500 axial scans per second," Opt. Express **16**(19), 15149–15169 (2008).
24. M. F. Kraus, B. Potsaid, M. A. Mayer, R. Bock, B. Baumann, J. J. Liu, J. Hornegger, and J. G. Fujimoto, "Motion correction in optical coherence tomography volumes on a per A-scan basis using orthogonal scan patterns," Biomed. Opt. Express **3**(6), 1182–1199 (2012).
25. M. F. Kraus, J. J. Liu, J. Schottenhamml, C.-L. Chen, A. Budai, L. Branchini, T. Ko, H. Ishikawa, G. Wollstein, J. Schuman, J. S. Duker, J. G. Fujimoto, and J. Hornegger, "Quantitative 3D-OCT motion correction with tilt and illumination correction, robust similarity measure and regularization," Biomed. Opt. Express **5**(8), 2591–2613 (2014).
26. F. LaRocca, D. Nankivil, S. Farsiu, and J. A. Izatt, "Handheld simultaneous scanning laser ophthalmoscopy and optical coherence tomography system," Biomed. Opt. Express **4**(11), 2307–2321 (2013).
27. Y. M. Liew, R. A. McLaughlin, F. M. Wood, and D. D. Sampson, "Motion correction of in vivo three-dimensional optical coherence tomography of human skin using a fiducial marker," Biomed. Opt. Express **3**(8), 1774–1786 (2012).
28. G. A. Holloway, C. H. Daly, D. Kennedy, and J. Chimoskey, "Effects of external pressure loading on human skin blood flow measured by 133Xe clearance," J. Appl. Physiol. **40**(4), 597–600 (1976).
29. W. J. Choi, H. Wang, and R. K. Wang, "Optical coherence tomography microangiography for monitoring the response of vascular perfusion to external pressure on human skin tissue," J. Biomed. Opt. **19**(5), 056003 (2014).
30. G. Pickering, D. Jourdan, A. Eschalier, and C. Dubray, "Impact of age, gender and cognitive functioning on pain perception," Gerontology **48**(2), 112–118 (2002).
31. K. M. Kennedy, L. Chin, R. A. McLaughlin, B. Latham, C. M. Saunders, D. D. Sampson, and B. F. Kennedy, "Quantitative micro-elastography: imaging of tissue elasticity using compression optical coherence elastography," Sci. Rep. **5**(1), 15538 (2015).
32. G. Lamouche, B. F. Kennedy, K. M. Kennedy, C.-E. Bisaillon, A. Curatolo, G. Campbell, V. Pazos, and D. D. Sampson, "Review of tissue simulating phantoms with controllable optical, mechanical and structural properties for use in optical coherence tomography," Biomed. Opt. Express **3**(6), 1381–1398 (2012).
33. Thorlabs, "NRT series motorized translation stage user guide," (2014).
34. C. Boudoux, "Field curvature," in *Fundamentals of Biomedical Optics: From Light Interactions with Cells to Complex Imaging Systems*, 1st ed. (Blurb, Incorporated, 2017), pp. 304–305.
35. W. M. Allen, K. M. Kennedy, Q. Fang, L. Chin, A. Curatolo, L. Watts, R. Zilkens, S. L. Chin, B. F. Dessauvagie, B. Latham, C. M. Saunders, and B. F. Kennedy, "Wide-field quantitative micro-elastography of human breast tissue," Biomed. Opt. Express **9**(3), 1082–1096 (2018).
36. P. Wijesinghe, D. D. Sampson, and B. F. Kennedy, "Computational optical palpation: a finite-element approach to micro-scale tactile imaging using a compliant sensor," J. R. Soc. Interface **14**(128), 20160878 (2017).
37. A. G. Podoleanu, "Optical coherence tomography," J. Microsc. **247**(3), 209–219 (2012).
38. R. W. Kirk, B. F. Kennedy, D. D. Sampson, and R. A. McLaughlin, "Near video-rate optical coherence elastography by acceleration with a graphics processing unit," J. Lit. Technol. **33**(16), 3481–3485 (2015).